1-30-2017

Finite Element Modeling of Fluid Flow, Thermal Transport, and Melt Pool Geometry in Metallic Powder Bed Additive Manufacturing Processes for Inconel 718

Richard E. Andreotta
University of Connecticut - Storrs, richard.andreotta@uconn.edu

Finite Element Modeling of Fluid Flow, Thermal Transport, and Melt Pool Geometry in Metallic Powder Bed Additive Manufacturing Processes for Inconel 718

Richard Andreotta

B.S., University of Connecticut, 2014

A Thesis

Submitted in Partial Fulfillment of the

Requirements for the Degree of

Master of Science

at the

University of Connecticut

2017

APPROVAL PAGE

Master of Science Thesis

Finite Element Modeling of Fluid Flow, Thermal Transport, and Melt Pool Geometry in Metallic Powder Bed Additive Manufacturing Processes for Inconel 718

Presented by

Richard Andreotta, B.S.

Major Advisor_____

Dr. Leila Ladani

Associate Advisor_____

Dr. Bi Zhang

Associate Advisor_____

Dr. Jafar Razmi

Associate Advisor_____

Dr. Tai-Hsi Fan

University of Connecticut

2017

Acknowledgements

I'd like to extend my sincere gratitude to the following people. Without their support and guidance this work would not have been possible.

Doctor Leila Ladani, my advisor, who provided me with support and guidance throughout my research. Her suggestions and constant help proved invaluable.

Magda Sadowski, my lab mate who patiently got me up to speed when I first started.

John Romano who's previous work gave me a sturdy foundation to build off of.

Pratt & Whitney who's funding and technical guidance made this project possible.

Table of Contents

List of Figures

List of Tables

Finite Element Modeling of Fluid Flow, Thermal Transport, and Melt Pool Geometry in Metallic Powder Bed Additive Manufacturing Processes for Inconel 718

Abstract

by

Rich Andreotta

The incorporation of a process's active physics as well as correct material properties into a model of that process is crucial as it limits assumptions and therefore the sources of error. In the case of laser melting (LM) processes current finite element models include only conductive heat transfer physics, and make assumptions to account for convective heat transfer within the melt pool, or neglect it entirely. Directly simulating conductive and convective heat transfer is needed to eventually create a truly robust model that accurately simulates reality. Furthermore there is a need for models that can predict the final shape of the bead cross section as it forms under surface tension and gravity forces. In this thesis the commercial finite element analysis software COMSOL Multiphysics is employed to model the laser melting process, including all relevant physics. Accurate thermal conductivity values measured through experiments up to 1000K are inputted into the model. In the first part of the model a set of Navier-Stokes equations and an energy balance are simultaneously solved to simulate both conductive and convective heat transfer. A cross section of the melted bead is then imported into the second part of the model which utilizes the level set method to track bead geometry as it forms under surface tension and gravity forces. The combination of these two simulations results in a predictive model that allows for the complete determination of final bead geometry, including bead height, and

directly simulates the convective flow within the melt pool in all three spatial dimensions. The model is validated by comparing predicted results with experimental melt pool and bead geometries of single line laser scans formed with a variety of process parameters. All experimental tracks were formed by an EOSINT M 280 using the same powder that was used for thermal testing. The culmination of this work is a first of its kind and highly sophisticated FE model of the powder bed laser melting process and an experimentally determined record of the thermal properties of gas atomized Inconel 718 powder.

Chapter 1. Introduction

1.1 Advantages

Additive manufacturing, more commonly known as 3D printing, refers to a variety of processes where three-dimensional objects are built one layer at a time. A 3D CAD model is segmented into the desired number of layers and each of these slices is built one on top of the other to make the final part. Historically, this technology was seen as a tool for rapid prototyping since additive processes are generally quicker, from conception to prototype, than their subtractive counterparts. A subtractive method such as machining, for example, involves cutting away unwanted material from a bulk solid. Depending on the desired geometry this can include turning, milling, drilling, or other operations. Furthermore, subtractive methods require multiple stages of production, including roughly shaping the bulk solid, performing initial cuts, and performing more detailed cuts for final precision or surface finishes. Often times these stages take place at different locations, adding transportation and scheduling costs. With additive manufacturing the part is built in one place and the same technique is used regardless of the part's geometry. Simply put the difference in build speed realized in certain applications stems from the adaptability of additive processes to complex build geometries. Recent advances in additive manufacturing technology have allowed for the rapid production of fully dense parts that satisfy desired mechanical properties with little or no post processing required. This technology promises significant benefits in the following areas:

1. Customized healthcare products
2. Reduced environmental impact
3. Simplified supply chain

The biomedical industry is especially affected due to the ability to create custom healthcare products. Implants and prosthetics can be customized based on an individual's needs without creating new molds for each patient. The simplified supply chain allows the onsite production of parts, which greatly reduces the cost and time involved in transporting a part to remote locations, such as a naval vessel or even the international space station. The environmental impact is reduced due to lower transportation costs and less wasted build material.

1.2 History

Two early roots of additive manufacturing can be identified: topography and photosculpture [1]. As early as 1890, a layered method was suggested for making molds for topographical relief maps. The method consisted of cutting wax plates along contour lines to create positive and negative three-dimensional surface molds. Paper maps could then be pressed into these molds to create a raised map. Photosculpture techniques were first proposed in 1860 as a way to create exact three-dimensional replicas of any object. The technique consisted of placing 24 cameras equally around the circumference of an object. An artisan would then carve 24 cylindrical portions of the figure using the silhouette of each photograph. Eventually, photosensitive gelatin and filtered light were incorporated to make the process less labor intensive. The two techniques have little in common with modern additive processes, but they represent the starting point of layer by layer manufacturing.

The first modern additive manufacturing technique to achieve commercial viability was stereolithography, developed by 3D Systems in 1986 [2]. This technique produces parts layer by layer using photopolymerization, a process by which light causes molecular chains to link together, forming polymers. The technique starts with a pool of photosensitive material being exposed to an ultraviolet laser. The laser is pre-programmed based on a Stereolithography file

(STL) to polymerize the desired shape of the first layer. Then the elevator apparatus is dropped a distance equal to one layer thickness and a resin-filled blade sweeps across the previous layer, re-coating it with material. This sequence is continued until the part is complete. These types of methods are often referred to as a top down technique, because the build plate drops down to accommodate each new layer. Bottom up techniques also exist in which the laser is focused upwards through the bottom of a vat that is filled with photosensitive emulsion. The rest of the process is similar except the part is pulled upwards through the vat. Next came fused deposition modeling (FDM) and laminated object manufacturing (LOM), both introduced in the late 1980's [3]. Fused deposition modeling, like all modern additive manufacturing techniques, starts with a software process by which a CAD file is mathematically sliced and oriented. These slices are stored in a file format called STL, which stands for STereoLithography file format. The part is then produced by extruding small strings of molten material to form layers of the final part. The material supply comes from a wound wire that is liquefied before passing through the nozzle and solidifies shortly afterward. The strings are often deposited in a crisscross fashion to combat anisotropic effects [4]. Laminated object manufacturing is a rapid prototyping process developed by Helisys Inc. In LOM, layers of adhesive-coated paper, plastic, or metal laminates are cut to shape based on an STL file. Then layers are successively glued together to form the final part. LOM results in parts with low internal tensions, high durability, and a wide range of possible sizes. Disadvantages include low accuracy in the vertical direction due to swelling effects, and inhomogeneity in thermal properties due to the adhesive coating between layers of laminate [5]. The next major advancement in additive manufacturing technology was the powder-bed based processes. Selective laser sintering (SLS) was first patented by Ross Householder in 1979. Although being patented 13 years earlier, the process wasn't sold commercially until 1992 by

DTM Corporation [4]. It involves a powdered layer being selectively sintered by an energy source, usually a laser or electron beam. When the first layer is complete the build platform is dropped one layer thickness, a new layer of powder is raked over the previous layer, and the process repeats until the part is complete. The distinction between sintering and melting sits in the quantity of energy that's imparted on the powder bed. Sintering processes use comparatively low energy sources, resulting in necking between powder particles, which is different from melting processes in which full melting occurs [6]. A diagram of necking between particles is shown below.

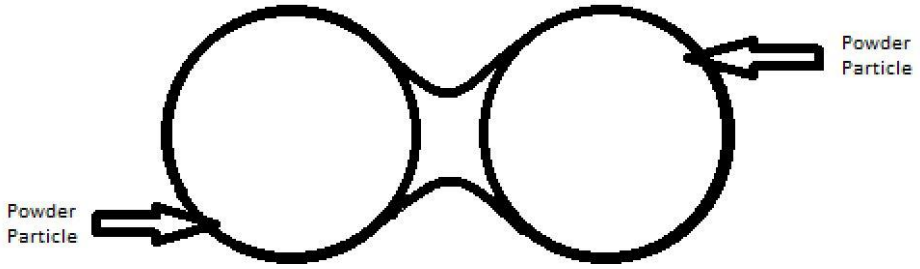

Fig. 1. Necking of two powder particles during sintering process.

At first the only available material was a polymer powder, but since then the range of available materials has widened, now including a variety of powdered metal alloys. Metallic powder-bed based processes can be divided into two categories: material binder and melting/sintering. In material binder methods the powder bed consists of two materials, a binding material and a structural material. As the binder material is melted, capillary forces pull the molten binder through voids in the un-melted structural powder [7]. In melting/sintering methods only one material is present in the powder bed. The material is either sintered or fully melted to form a continuous layer. Sintering processes lead to parts that are high in porosities and exhibit low mechanical strength. In melting processes the powder is fully melted and manufactured parts have no or few porosities. Optimization parameters are crucial in full melting processes as the

higher temperatures lead to shrinkage and thermal distortion [8]. This research focuses on full melting processes as they allow production of fully dense parts with satisfactory mechanical strength.

1.3 Consolidation Phenomena

Kruth [9] presents an overview of the consolidation phenomena for various powder-bed based layered manufacturing processes. Solid state sintering (SSS) is a consolidation process that occurs below the powdered material's melting temperature. The particles exhibit necking behavior caused by the diffusion of atoms in solid state. The consolidation occurs in a temperature range between T_{melt} and T_{melt}, where T_{melt} is the melting temperature of the material. This mechanism is rarely applied in practice as the diffusion of atoms in solid state is a slow process and is not economically feasible. Liquid phase sintering (LPS) and partial melting processes include binding mechanisms where a portion of the powder is melted and a portion remains solid. This can occur when a binding material with a low melting temperature is included in the powder bed, or in a single composition alloy. When a powder is partially melted the portion that's liquefied spreads between solid particles almost instantaneously. This phenomenon allows for much higher scan speeds than SSS and is more economically feasible. Partial melting is also possible where no distinct binder and structural material are used. In this case, parameters are adjusted to only melt the outside of the powder particles, liquefying the outside and leaving a solid core. Then the liquefied material on each particle form necks between adjacent particles, acting as a binder material for the solid structural cores. Full melting is a consolidation mechanism that allows for the realization of fully dense parts without need for post processing. This advantage comes with a tradeoff, as full melting processes require careful process control to avoid defects [10]. The high temperature gradients and densification ratios

involved in full melting methods yield high internal stresses. There is also a risk of balling and dross formation in the melt pool [11]. Another problem associated with full melting processes is controlling the flow within the melt pool. The molten metal must sufficiently wet the previously solidified layer below it, and solidify in a way that its upper surface is flat enough to allow the next layer of powder to be spread over it. In the recent past, optimal operating parameters have been obtained experimentally for various materials. The aim of this research is to develop a model that allows for the realization of optimal parameters without the need for costly and time consuming experiments.

1.4 Flow Phenomena

This thesis aims to go beyond many existing models and include both fluid dynamics and heat transfer in the model's physics. Marangoni flow, also known as thermocapillary flow, is the dominant driving force of flow in the melt pool [12]. Buoyancy transport was also considered, but was ultimately ignored due to the melt pool being heated from the top. This conclusion is further supported by comparing the Marangoni number to the Grashoff number for average melt geometry and temperatures. The Marangoni number is 6-7 orders of magnitude higher than the Grashoff number, which supports the conclusion that thermocapillary flow is the dominant mechanism. Marangoni flow occurs when a surface tension gradient exists along the free surface of a liquid. Surface tension is a temperature dependent property so it follows that Marangoni effects will always occur when a temperature gradient exists at a liquid's free surface [13]. Marangoni convection is directed toward the regions of higher surface tension, so the sign of the surface tension coefficient will affect the direction of surface flow. Materials with a negative surface tension coefficient exhibit increased surface tension as temperature decreases, driving flow toward the lower temperature areas. Most materials used in laser melting processes have a

negative surface tension coefficient, which acts to drive flow toward the periphery of the melt pool. In general, the flow pattern within the melt pool can be represented by the diagram below.

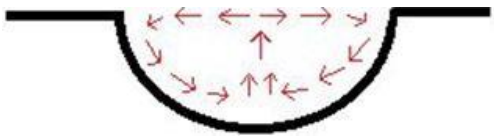

Fig. 2. Typical flow field in melt pool cross section.

Along the free surface of the melt pool the highest temperature (and lowest surface tension) is located in the middle, due to the laser's peak intensity occurring at the center of its circle of influence. The edges of the melt pool are also heated by the laser, but the laser's intensity decreases radially from its center, which results in lower temperatures (and higher surface tension) at the melt pool's edges. This surface tension gradient acts to pull the molten metal away from the center of the melt pool. This is supported by Chan [14] who developed a three dimensional model of the thermocapillary flow within laser melt pools. Raghavan [15] used a well-tested model of the laser melting process to show that Marangoni convection is the dominant flow mechanism, and also used the Peclet number to show that convective heat transfer cannot be neglected. This paper will also use the dimensionless Peclet number to quantify the importance of conductive vs convective heat transfer in additive manufacturing processes.

1.5 Operating Parameters

It is important to understand the effects of various process parameters, especially in full melting processes. Currently these parameters must be optimized for each material, experimentally, before the material is ready for use in commercial production. One of the aims of this work is to develop a model that can predict ranges of optimal parameters to lessen the need for costly

experiments. To begin, it is necessary to understand the effects of changing each parameter while keeping all others constant.

- Preheat Temperature: Higher preheat temperatures lead to smaller thermal gradients. This results in less thermal stresses and favors equiaxed grain structures [16].
- Beam Diameter: A larger beam diameter means the beams intensity is spread over a larger area. This leads to lower maximum temperatures and less beam penetration [16].
- Scan Speed: Higher scan speed means less energy is imparted onto the powder bed. This means less melting and lower part density [17].
- Layer Thickness: Increasing layer thickness will decrease build times, but sacrifices accuracy in the vertical direction.
- Powder Particle Size Distribution: Smaller particles lead to less porous powder beds. This leads to heat being dissipated more readily which means lower temperatures and less melting [17].
- Beam Power: Higher beam power leads to higher temperatures, more penetration, and more melting [19].

The literature contains many studies, both modeling and experimental, that quantify the effects of altering these process parameters. Mohanty [20] used a combined modelling-experimental approach to predict a range of outputs for varying process parameters, and used a Monte Carlo method based uncertainty analysis methodology to establish the reliability of the process. Yadroitsev [18] used experimental results combined with a factor analysis to investigate the effects of various process parameters on cross-sectional geometry of single line scans. Both authors work agreed with the summary of process parameters presented above, and in general are quite intuitive. Any alteration that leads to an increase in overall energy, including increased

beam power or decreased scan speed, acts to raise the peak temperature of powder bed. In most cases this leads to more complete melting and a denser part, however when the temperature is increased beyond a certain threshold vaporization and loss of mass can occur. In addition to energy considerations, layer thickness particle size distribution have predictable effects. Layer thickness is directly correlated to bead height, and is the main contributor to bead height determination. A smaller particle size distribution means less void space within the powder bed which increases the rate of heat dissipation and produces lower peak temperatures. Particle size distribution also has a role in absorptivity considerations, but that type of analysis is outside the scope of this thesis and will not be considered in this work.

1.6 Gaps in Literature

There is still a need for models with correct material properties and coupled heat transfer and computational fluid dynamics that are capable of predicting complete melt pool geometry. Most models in the literature only consider conductive heat transfer and make assumptions to account for convection. Furthermore the thermal conductivity of powder material is often derived theoretically from bulk solid values. This researcher aims to better simulate reality by developing a more complete finite element model with less assumptions that uses experimentally determined values of thermal conductivity.

1.7 Objectives

The objective of this thesis is to move beyond existing models by coupling CFD with heat transfer physics in an attempt to model both conductive and convective thermal transport. Furthermore, this model will track the interface between the molten bead and surrounding atmosphere as it forms under surface tension forces and solidifies into its final geometry. This will allow for a better selection of process parameters and a final part that is more accurate in the

vertical direction. This thesis will also provide thermal properties of Inconel 718 powder, determined at a range of temperatures and densities with a TPS 2200.

Chapter 2. Modeling Setup

2.1 Literature Review

Yadroitsev and Yadroitsava [18] performed a factor analysis of SLM process parameters by analyzing the results of 18 different single line scans. Their analysis showed that laser power is the dominant parameter effecting melt pool width, melt pool depth, and contact angle. The top contributor to bead height is layer thickness, which also has a significant impact on melt pool depth. Their analysis also showed that powder size distribution has a significant effect on bead height, but virtually no effect on melt pool width. Fu and Guo [21] developed a 3-dimensional finite element simulation to model multi-layer deposition of Ti-6Al-4V in selective laser melting. Their model concluded that both melt pool depth and volume increase with increased laser power or decreased scan speed. Their simulations also suggest that for a given laser power a powder bed will experience higher temperatures and melting than a solid substrate. This difference is due to the lower thermal conductivity of the powder, which results in slower dissipation of heat which allows for highly localized heat deposition and more extensive melting. Boley and Khairallah [22] used a packing algorithm and ray tracing software to investigate the absorptivity of metal powders. They concluded that optimal packing can increase absorptivity by a factor of two, compared to the random packing methods employed by SLM machines. This finding suggests that even with identical operating parameters two scans may differ significantly. Roberts and Wang [23] utilized a method called element birth and death to simulate the practical layer-wise build process that is undergone in actual additive part production. They used a time delay of 1 second in-between successive powder coatings and found that previous layers

experienced secondary temperature spikes due to the scanning of new layers. They also found a small but incremental temperature build up in the part and in the baseplate as more layers were scanned. Foroozmehr and Badrossamy [24] developed a finite element model that considered penetration depth of the heat source. Results found good agreement with melt pool dimensions, however Marangoni convection was ignored.

Inconel 718 was chosen as the focus of this work due to its increasing importance in the development and manufacture of jet engines, mainly due to its high strength and temperature resistant properties [25]. Inconel 718 also exhibits good corrosive properties [26] which makes it an ideal choice for the aerospace industry. Due to its low machinability [27] this researcher emphasizes the importance of research into additive manufacturing techniques.

2.2 Governing Equations

Many studies in the literature present models that omit fluid flow from their representative physics. This exclusion adds complexity to the modeling setup, as thermal transport due to convection must be accounted for in some other way. There is also thermal transport via radiation between individual powder particles. Tolochko [28] introduced an effective thermal conductivity to account for radiation, convection, and conduction. The model presented in this thesis does not need an effective thermal conductivity since convection will be accounted for by the inclusion of CFD in the model, and radiation and conduction will be accounted for in the determination of thermal properties with the TPS 2200.

The simulation presented in this thesis is the result of two separate models created in Comsol Multiphysics. The first model is three-dimensional and consists of three rectangular boxes which make up a powder, solid, and build plate domain. Each domain is a rectangular box, with the

powder domain stacked on top of the solid domain which is stacked on top of the build plate. The powder domain represents a fresh powder layer while the solid domain represents previously built layers. All side walls and the bottom of the build plate are given an adiabatic boundary condition. The top surface was given a diffuse radiation boundary condition as there is heat loss due to radiation on the top surface. The model uses a Gaussian distributed heat source to model the laser and is passed over the length of the powder layer at the desired scan speed. As this happens, COMSOL tracks and stores melt pool geometry and temperature data.

The second model is two-dimensional and is used to simulate the melt pool deformation into a bead shape due to surface tension forces. It uses the level set method to track the interface between the molten bead and the surrounding atmosphere. The geometry of the molten bead and the temperature dependent dynamic viscosity are imported from the first model. Model number two starts as the melt pool approaches melting temperature and ends when it drops below melting temperature. By using temperature dependent dynamic viscosity the solidification is modeled. All equations are taken directly from the COMSOL Multiphysics documentation [29].

Model one consists of three rectangular boxes which make up a powder, solid, and build plate domain. Figure 3 depicts the model setup with the powder domain stacked on top of the solid domain which is stacked on top of the build plate. The dimensions of each domain are specified in Table 1, where the Y-dimension is halved in the model's geometry due to planar symmetry. The powder domain, solid domain, and build plate domain represent the fresh powder layer, previously built layers, and the build plate, respectively. All side walls and the bottom of the build plate were given an adiabatic boundary condition because a single line laser scan is a highly localized event. The top surface was given a diffuse surface boundary condition to represent heat loss due to radiation. Boundary conditions can be seen in figure 3, where slip

refers to a boundary velocity condition. The slip condition is somewhat arbitrary due to the high dynamic viscosity of all elements near the boundary. The equations governing each boundary condition are shown in Table 2. The equations in Table 2 make use of the following variables: $\boldsymbol{n}$: Vector normal to surface, $\boldsymbol{q}$: Heat flux, ε: Emissivity, σ: Stefan-Boltzmann constant, $\boldsymbol{u}$: Velocity, $\boldsymbol{K}$: Viscous stress tensor, γ: Surface Tension Coefficient, T_x and T_y: X and Y partial derivatives of temperature, **u** and **v**: X and Y components of velocity. The mesh consists of cubic elements with 20 micron side length along the lasers path and large tetrahedral elements away from the laser. The completed mesh consists of 168,000 elements.

Table 1. Dimensions of Domains in Model One

Domain	X (mm)	Y (mm)	Z (mm)
Powder	9	3	.04
Solid	9	3	.9
Build Plate	9	3	1

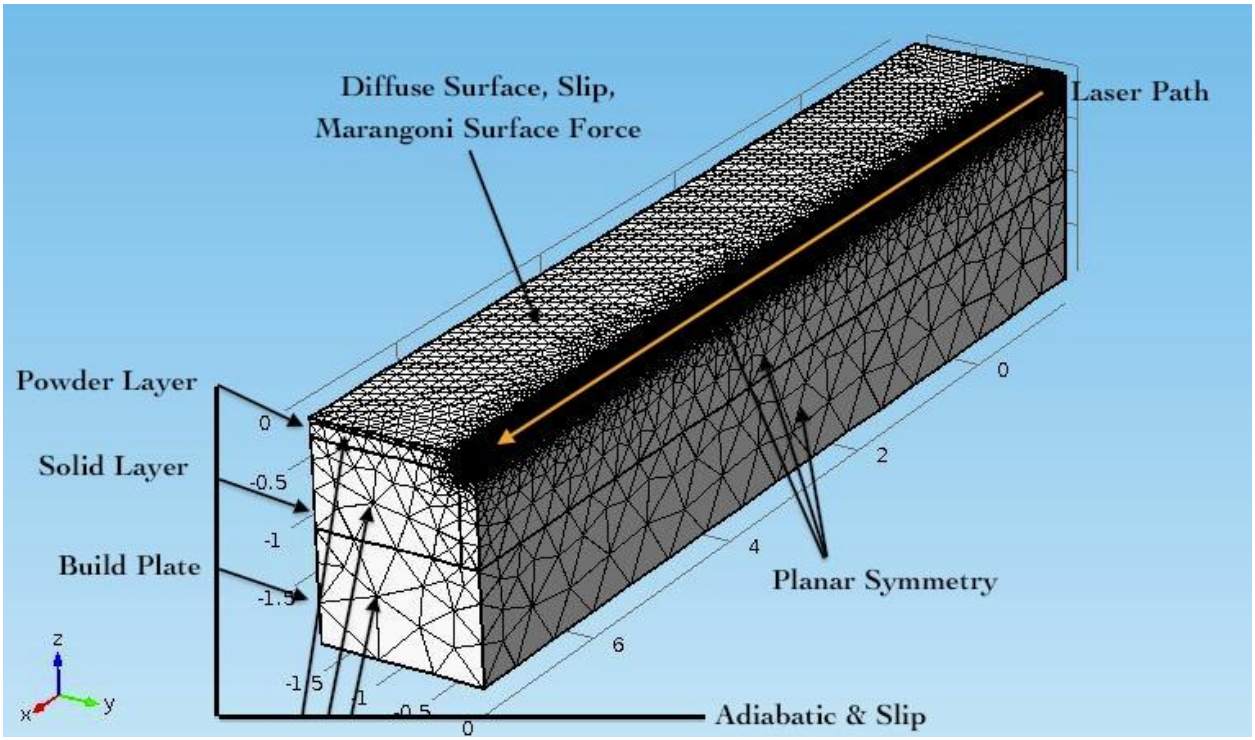

Fig. 3. Meshed Model Geometry with Boundary Conditions

Table 2. Boundary Conditions and Corresponding Equations

Boundary Condition	Governing Equation
Adiabatic	$-\boldsymbol{n} \cdot \boldsymbol{q} = 0$
Diffuse Surface	$-\boldsymbol{n} \cdot \boldsymbol{q} = \varepsilon\sigma(T_{amb}^4 - T^4)$
Slip	$\boldsymbol{u} \cdot \boldsymbol{n} = 0$
Marangoni Force	$\boldsymbol{F} = \text{test}(\mathbf{u}) * \gamma * T_x + \text{test}(\mathbf{v}) * \gamma * T_y$

To calculate temperature, velocity, and pressure fields an energy balance, momentum balance, and mass balance were included. The energy balance is given by equation 1 where the conductive heat flux, $\boldsymbol{q}$, is given by $\boldsymbol{q} = -k\nabla \boldsymbol{T}$.

$$\rho C_p \frac{\partial \boldsymbol{T}}{\partial t} + \rho C_p \boldsymbol{u} \cdot \nabla \mathbf{T} + \nabla \cdot \mathbf{q} = \mathbf{Q} \qquad \textit{Eq. 1}$$

Equation 1 includes the following parameters and variables: $\boldsymbol{u}$: The velocity field, **Q**: The heat source, **T**: The temperature field, ρ: The density, C_p: The heat capacity. The velocity term comes from the mass and momentum balances while the heat source represents the laser beam. The heat source was specified as a three dimensional function that decays radially outward from the center and linearly parallel to the beam. The radial decay was specified by a Gaussian distribution with a standard deviation equal to one third of the effective beam radius, which ensures 99.7% of the laser energy is accounted for. The linear decay was specified by a linear function valued one at the surface and zero at the penetration depth. The momentum and mass balance are represented below by equations 2 and 3.

$$\rho \frac{\partial \boldsymbol{u}}{\partial t} + \rho(\boldsymbol{u} \cdot \nabla)\boldsymbol{u} = \nabla \cdot [-p\boldsymbol{I} + \mu(\nabla \boldsymbol{u} + (\nabla \boldsymbol{u})^T)] + \boldsymbol{F} \qquad \textit{Eq. 2}$$

$$\rho \nabla \cdot (\boldsymbol{u}) = 0 \qquad \textit{Eq. 3}$$

Equations 2 and 3 make use of the following variables and parameters: μ: The dynamic viscosity, p: The pressure, $\boldsymbol{I}$: The identity matrix. In equation 2 the $\boldsymbol{F}$ term allows for the inclusion of surface and body forces, which is where surface tension gradient driven Marangoni forces were specified as a weak contribution to the source term as shown in Table 2. The test functions are the heart of the weak form, which turns differential equations into integral equations. The test functions sample values at infinitesimal intervals to negate the need for second derivative continuous dependent variables. Integrations by parts is then used to reduce the order of integration and provide a numerical advantage [29]. Model two is two dimensional and consists of two domains which represent the ambient atmosphere and the molten bead cross

section. Molten region geometry was imported from model one and the level set method was used to track the free surface of the bead as it deforms to its equilibrium state under gravity and surface tension forces. Solidification time was also computed using temperature history from model one and is incorporated into model two with a time dependent dynamic viscosity. Model two includes the same mass and momentum balances from model one, as well as equations 4 through 6, which solve for the initial interface position and track its evolution.

$$\nabla Gl \cdot \nabla Gl + \sigma_w Gl(\nabla \cdot \nabla Gl) = (1 + 2\sigma_w)Gl^4 \qquad \textit{Eq. 4}$$

$$l_w = \frac{1}{Gl} - \frac{l_{ref}}{2} \qquad \textit{Eq. 5}$$

$$\frac{\partial \phi}{\partial t} + \nabla \cdot (\boldsymbol{u}\phi) = \lambda \nabla \cdot \left(\epsilon_{ls} \nabla \phi - \phi(1 - \phi) \frac{\nabla \phi}{|\nabla \phi|} \right) \qquad \textit{Eq. 6}$$

Equations 4 through 6 make use of the following variables and parameters: Gl: Reciprocal interface distance, σ_w: Surface tension coefficient, l_w: Initial interface distance, l_{ref}: Reference length $\boldsymbol{u}$: The velocity field, λ: Reinitialization parameter, ϵ_{ls}: Parameter controlling interface thickness, ϕ: The level set variable. For each time step the level set variable is solved for both domains. The value of the level set variable in each domain is negative or positive, and zero over the interface, as depicted in figure 4. The interface thickness is set to half the maximum element size, and the reinitialization parameter is set to 0.4 which is sufficiently close the maximum

interface velocity, as is recommended in the COMSOL documentation. The contact angle between both fluids and the underlying substrate is inputted as is required by the level set method. Contact angle was calculated by taking an average of 10 experimental tracks formed by and EOSINT M 280 for each set of process parameters. Figure 6 shows the mesh density analysis for model one. An average mesh density of 4834 elements per cubic millimeter was used since increasing the mesh density yielded no significant change in maximum temperature. Refining the mesh in model two did not change results.

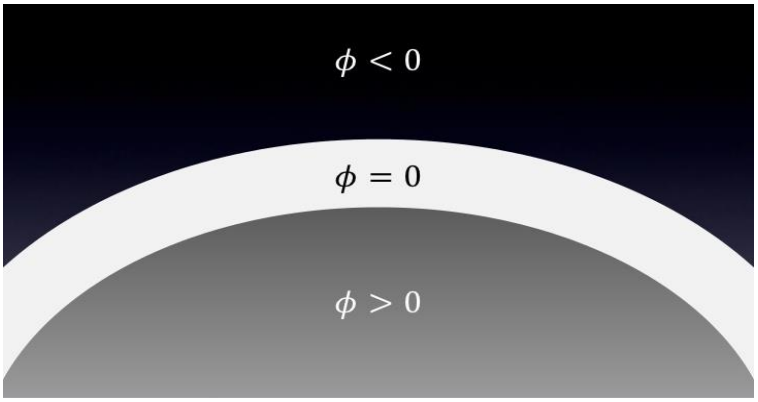

Fig. 4. Level Set Method

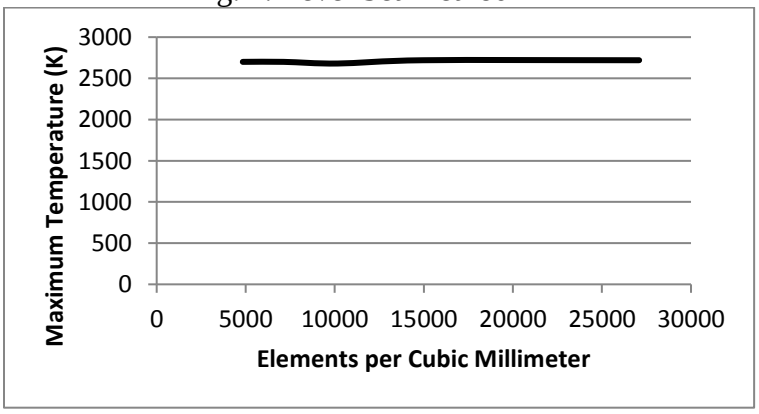

Fig. 5. Mesh Density Analysis

Chapter 3. Material Properties

3.1 Thermal Conductivity

Thermal conductivity was measured with a TPS 2200 scientific instrument. The instrument is designed to non-destructively measure the thermal properties of solid, liquid, paste, and powdered materials. It claims accuracy of 2% for thermal conductivity and 5% for specific heat capacity. The instrument relies on a method which utilizes a sensor element in the shape of a double spiral which simultaneously supplies heat to the sample and measures the time dependent temperature increase. The sensor is made of a 10 um thick Nickel-metal double spiral encapsulated by Mica, which electrically insulates the spiral and provides it with mechanical strength. The TPS 2200 was used with a 4L muffle furnace to make measurements at 50 degree intervals up to 1000K. Five measurements were taken at each temperature, and powder mass and chamber volume were measured after each run to calculate packing density. The values obtained with a packing density consistent with a 0.3 porosity assumption were the ones ultimately used in simulations. A figure and a full list of values can be found in Appendix A.

3.2 Heat Capacity

Heat capacity values were taken directly from Mills [30]. Latent heat of fusion is included by the apparent heat capacity method [29]. The temperature transition zone is defined as $\Delta T = T_{liq} - T_{sol}$. From Mills [30], $T_{sol} = 1443K$ and $T_{liq} = 1609K$. The method is summarized in Table 3, and Fig. 6-Fig. 7 below. In the following table C_p is the specific heat and L_f is the latent heat of fusion of Inconel 718.

Table 3. Summary of Apparent Heat Capacity Method

Specific Heat	Temperature Range
$C_p = C_p(T)$	$0 \leq T \leq T_{sol}$
$C_p = C_p(T) + \frac{L_f}{\Delta T}$	$T_{sol} \leq T \leq T_{sol} + \Delta T$
$C_p = C_p(T)$	$T_{liq} \leq T$

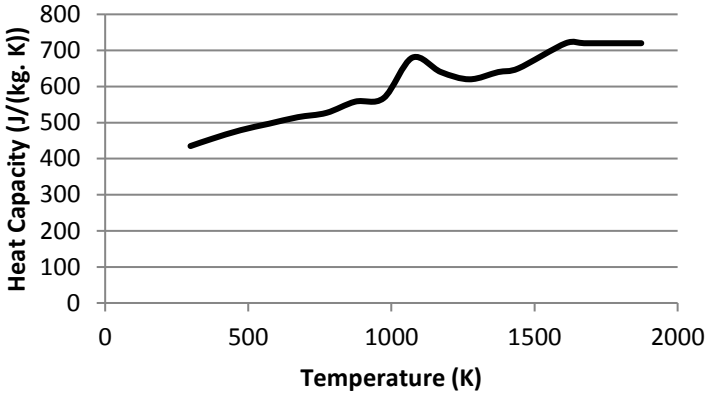

Fig. 6. Heat Capacity of Inconel 718

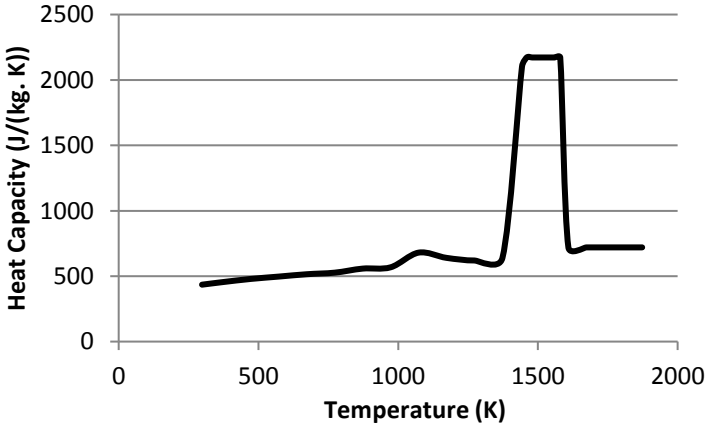

Fig. 7. Apparent Heat Capacity of Inconel 718

A full list of values can be found in appendix A.

3.3 Density

Density values of solid Inconel 718 were taken directly from Mills [30], and the powder values were obtained by assuming a porosity of 0.3. A figure and full list of values can be found in appendix A.

3.4 Dynamic Viscosity

Dynamic viscosity values were calculated using a parameterized equation proposed by Andon and Day [31], which is labeled equation 7 and shown below. Temperature is in Kelvin.

$$\mu\ (mPa * s) = 0.196e^{\frac{5848}{T}} \qquad \textit{Eq. 7}$$

A figure and full list of values can be found in appendix A.

3.5 Absorptivity

A value of 48% was used, as experimentally determined by Haq, Shah, and Khan [32].

3.6 Emissivity

A predictive model proposed by Sih and Barlow [33] was used to predict effective emissivity of the powder bed. The model consists of three equations, labeled equations 8, 9, and 10.

$$\varepsilon = A_h\varepsilon_h + (1 - A_h)\varepsilon_h \qquad \textit{Eq. 8}$$

$$A_h = \frac{.908p^2}{1.908p^2 - 2p + 1} \qquad \textit{Eq. 9}$$

$$\varepsilon_h = \frac{\varepsilon_s\left[2 + 3.082\left(\frac{1-p}{p}\right)^2\right]}{\varepsilon_s\left[1 + 3.082\left(\frac{1-p}{p}\right)^2\right] + 1} \qquad \textit{Eq. 10}$$

The previous equations include the following parameters: ε: The effective emissivity, ε_h: The emissivity of the cavities, ε_s: The emissivity of the bulk material, A_h: The area fraction of surface occupied by cavities, p: The powder bed porosity. A porosity of 30% is assumed in accordance with the literature, and a solid emissivity of 85% is used as reported by Greene and Finfrock [34]. The resulting effective emissivity is 87%.

Chapter 4. Results

4.1 Thermal Conductivity Measurements

Measurements were taken at three different packing densities with the least dense not being packed down at all. The results are shown below in figure 8.

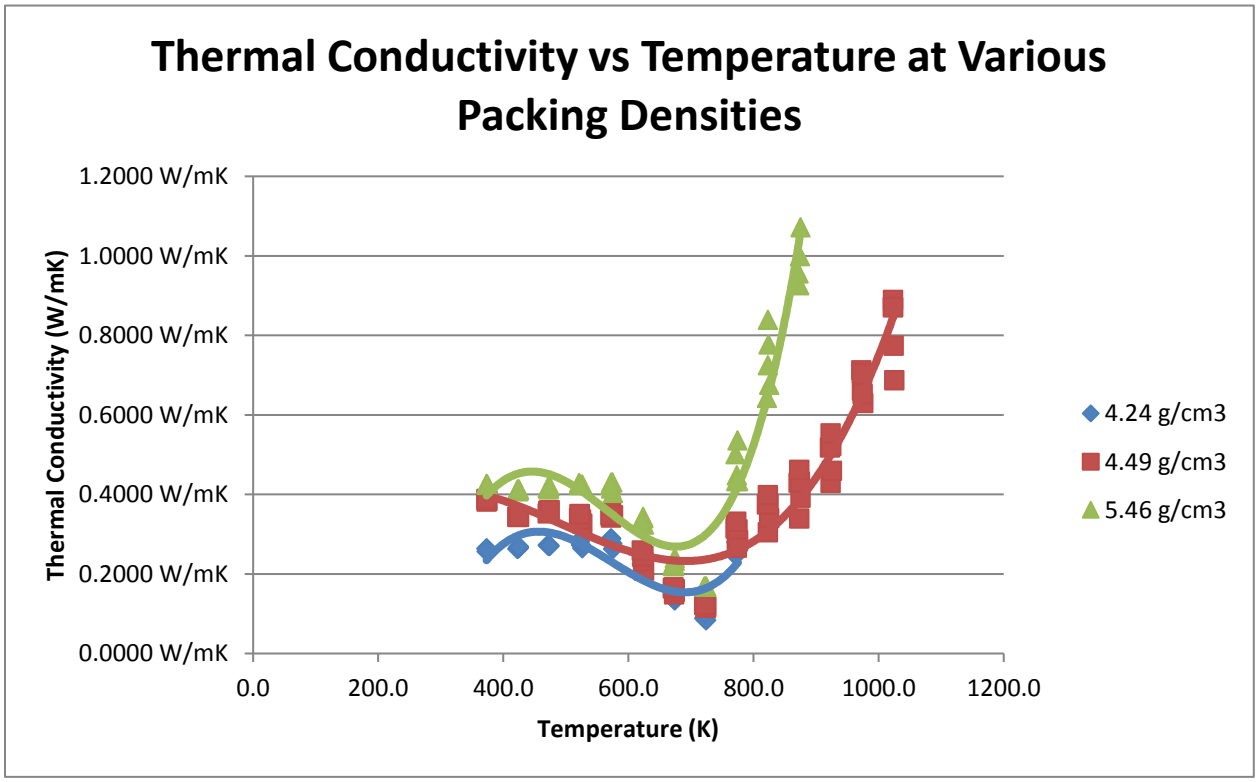

Fig. 8. Thermal Conductivity vs Temperature

Only one of the packing densities was measured up to 1000K due to running out of compressed nitrogen gas. Although the other two densities could only be measured to around 800K, the trend lines allow for the extrapolation of values up to the melting point at 1443 K. For all three densities measured there is a clear minimum between 600K and 800K. This can be explained by examining the thermal conductivity of pure nickel which also experiences a minimum between 600K and 800K. Inconel 718 is comprised of between 50 and 55 percent nickel, so these results can be expected. The values obtained for the highest packing density tested, 5.46 g/cm^3 were used in the model because that density corresponds to a porosity of .67 which is closest to .7, which is the most often assumed porosity of powder beds in the literature. Each set of values was tested in the model but the conductivities were close enough that no significant change in predicted melt pool geometry or maximum temperature was detected.

4.2 Simulation Results

The validity of the model was tested by comparing predicted and experimental results at 12 different sets of operating parameters. The parameters are shown in Table 4. Only parameters that resulted in a stable and consistent melt pool were considered.

Table 4. Process Parameters Considered

	100W	150W	200W	300W
200 mm/s	Yes	Yes	Yes	Yes
700 mm/s		Yes	Yes	Yes
1200 mm/s		Yes	Yes	Yes
2200 mm/s				Yes
2500 mm/s				Yes

The model offered good predictions for melt pool width as can be seen in figure 9 and table 5 below.

Table 5. Comparison of Experimental and Simulation Results for Average Melt Pool Width

Simulation (um)					Experiment (um)					Percent Difference				
Average Width	100W	150W	200W	300W	Average Width	100W	150W	200W	300W	Average Width	100W	150W	200W	300W
200 mm/s	184	231	290	370	200 mm/s	154.2 +- 14.6	204.3 +- 11	223.3 +- 14.8	295.1 +- 23.9	200 mm/s	-19.33%	-13.07%	-29.87%	-25.38%
700 mm/s		124	132	194	700 mm/s		118 +- 5.1	144.5 +- 9.2	185 +- 12.1	700 mm/s		-5.08%	8.65%	-4.86%
1200 mm/s		113	118	146	1200 mm/s		97 +- 8.1	113.6 +- 11.9	132 +- 10.6	1200 mm/s		-16.49%	-3.87%	-10.61%
2200 mm/s				116	2200 mm/s				104 +- 9	2200 mm/s				-11.54%
2500 mm/s				112	2500 mm/s				94 +- 16.9	2500 mm/s				-19.15%

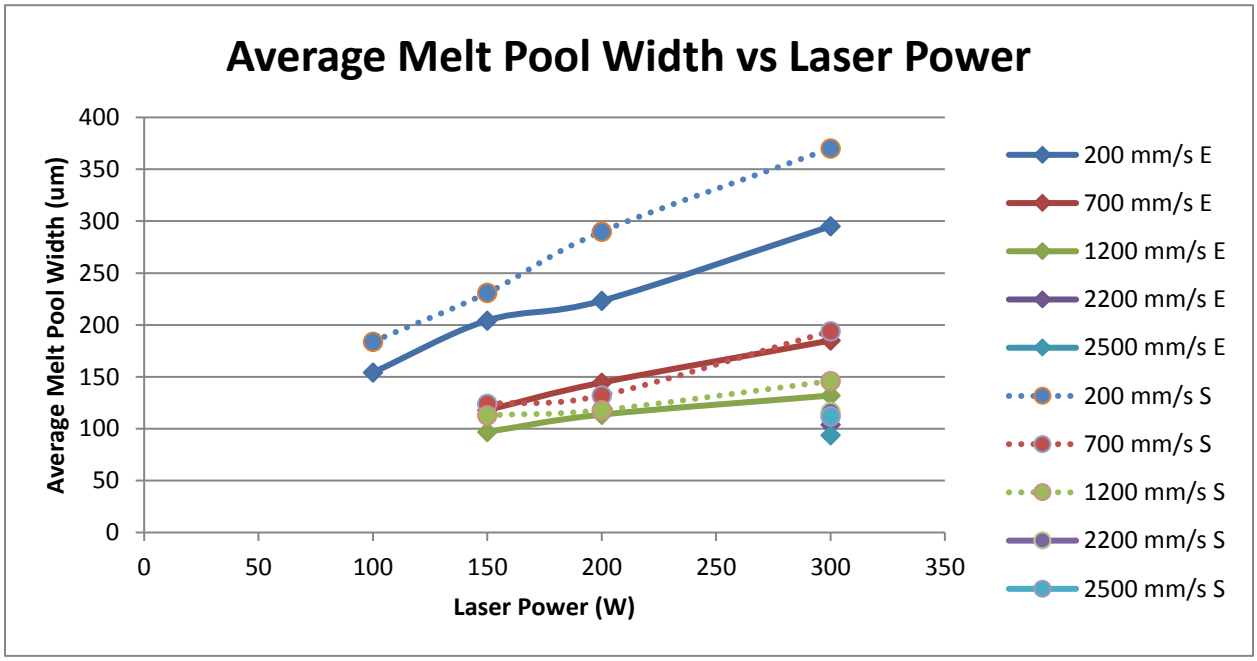

Fig. 9. Average Melt Pool Width vs Laser Power

The model performed best at higher scan speeds achieving an average error of 10.03% at scan speed of 700 mm/s or higher. Even when all scan speeds are considered the model predicts melt

pool width with a reasonable average error of 14%. Similar figures and tables for melt pool depth are shown below.

Table 6. Comparison of Experimental and Simulation Results for Melt Pool Depth

Simulation (um)					Experiment (um)					Percent Difference				
Melt Pool Depth	100W	150W	200W	300W	Melt Pool Depth	100W	150W	200W	300W	Melt Pool Depth	100W	150W	200W	300W
200 mm/s	87	115	134	165	200 mm/s	148.1 +- 40.3	215.7 +- 67.5	280.5 +- 48.6	299.1 +- 149	200 mm/s	41.26%	46.69%	52.23%	44.83%
700 mm/s		42	60	93	700 mm/s		48.2 +- 11.3	64.4 +- 18.2	96.5 +- 24.7	700 mm/s		12.86%	6.83%	3.63%
1200 mm/s		10.5	41	66	1200 mm/s		34 +- 14.2	41.5 +- 9.8	101.1 +- 37.2	1200 mm/s		69.12%	1.20%	34.72%
2200 mm/s				37	2200 mm/s				42.7 +- 8.8	2200 mm/s				13.35%
2500 mm/s				19	2500 mm/s				39.9 +- 14.8	2500 mm/s				52.38%

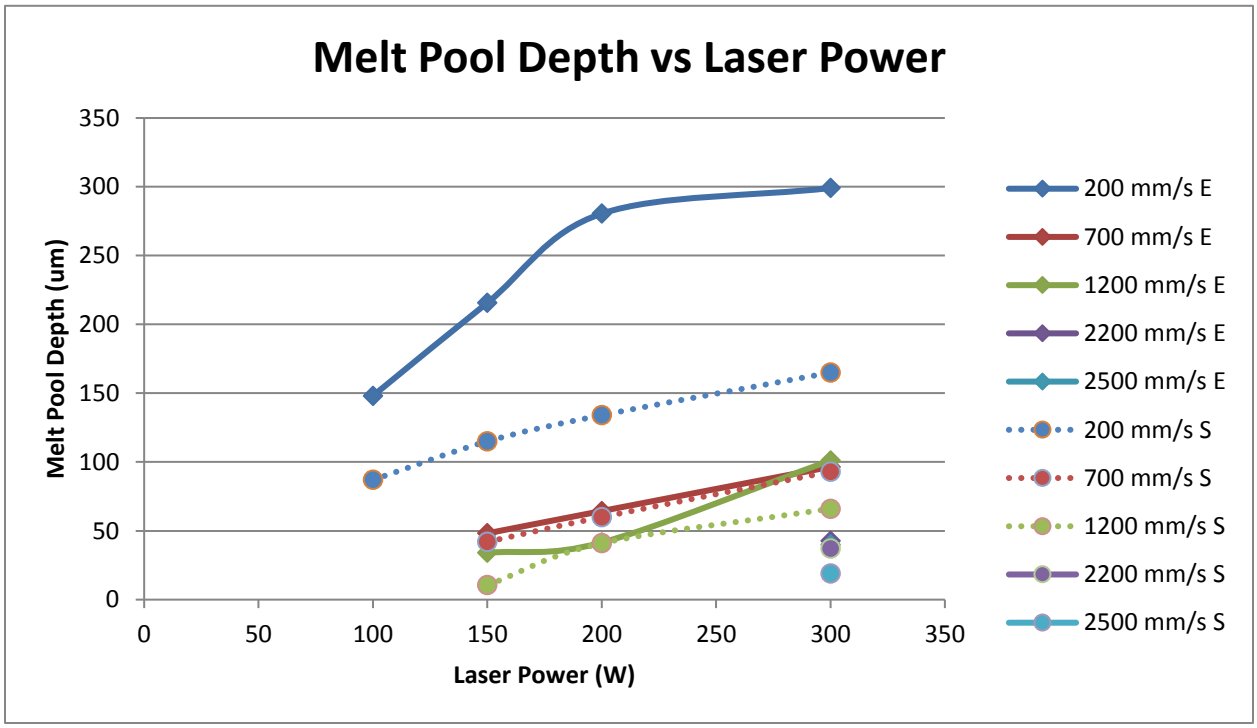

Fig. 10. Melt Pool Depth vs Laser Power

Table 6 and Figure 10 show reasonable agreement between simulation and experimental results except at a scan speed of 200 mm/s where the error is more pronounced. At a 700 mm/s scan speed the average error is 7.77%. The average error for all scan speeds except 200 mm/s is 24.27%. This is in stark contrast to the average error at scan speeds of 200mm/s which is 46.1%.

The consistently high errors at scan speeds of 200 mm/s, as well as the high penetration depths of experimentally formed scans at that scan speed lead this researcher to believe that it is possible a peculiarity of the machine these experimental tracks were formed on is partly to blame for the error. This assertion is supported by the high standard deviation of the 200 mm/s 300W scan as can be seen in table 6. It is known that the random packing of powder particles causes some natural deviation, however these experimental averages were taken from measurements of 10 individual scans and a standard deviation that is 50% of the mean seems questionable. Experimental measurements of bead height were only available for 4 sets of process parameters due to the balling effect, or error in the cross section and polishing process. Figure 11 shows 4 examples of experimentally obtained cross sections. The top two were omitted from bead height measurements while the bottom two were considered.

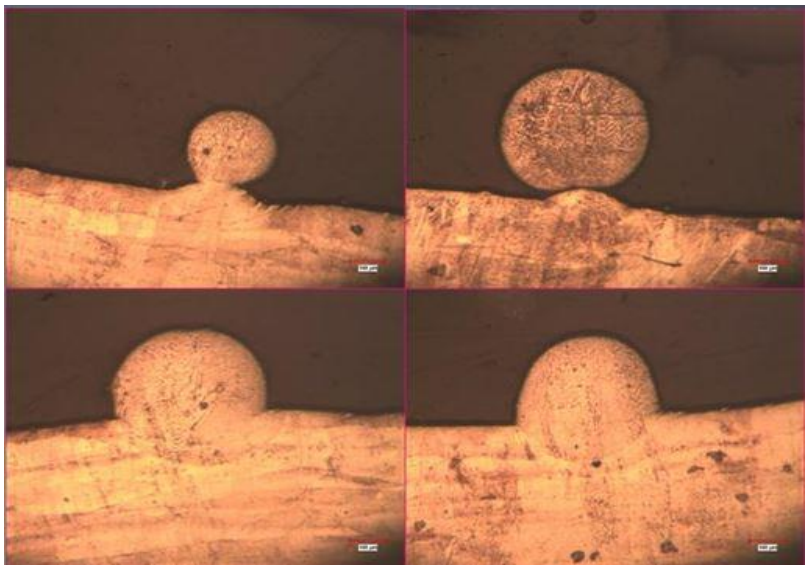

Fig. 11. Examples of Polished Cross Sections

A comparison of experimental and simulation results for bead height is shown in figure 12.

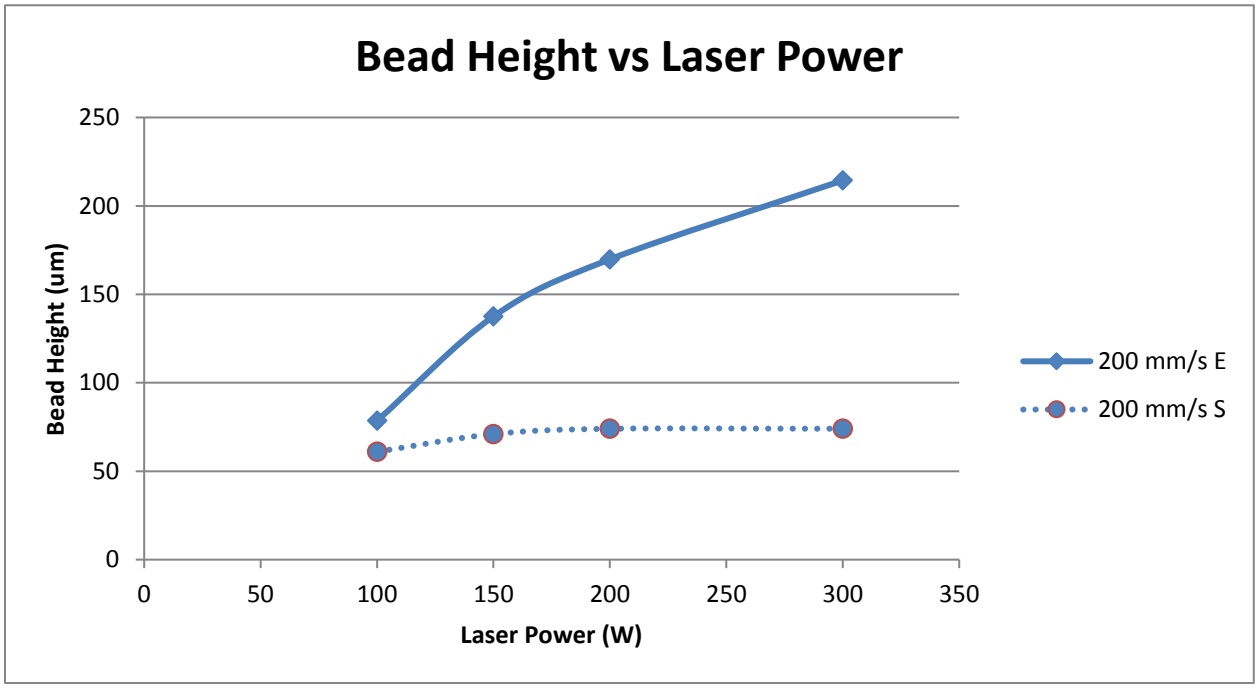

Fig. 12. Bead Height vs Laser Power

It is clear from figure 12 that the model offered no useful prediction regarding the bead height if experimentally formed tracks. This could be for a variety of reasons. First of all as previously stated, the experimental results suggest some experimental error during the formation of the 200 mm/s scan speed tracks. The literature consistently shows that bead height closely mimics layer thickness and can be at most double the layer thickness. All experimental tracks were formed using a layer thickness of .040 mm, which casts doubt on the validity of the tracks formed at 200 mm/s and 300W, the average bead height of which exceeds .200 mm. The discrepancy is most likely also due to the fact that powder sucked into the melt pool was not incorporated in this model. It is a documented phenomenon that powder at the edge of the melt pool can be pulled

into it due the mixing caused by thermocapillary forces. This researcher still asserts that the model's predictions of bead height which is based on the contact angle and surface tension values of a molten Inconel 718 and Nitrogen interface are valid.

Figure 13 shows a cross section of the melt pool where the flow within the melt pool is represented by an arrow velocity plot.

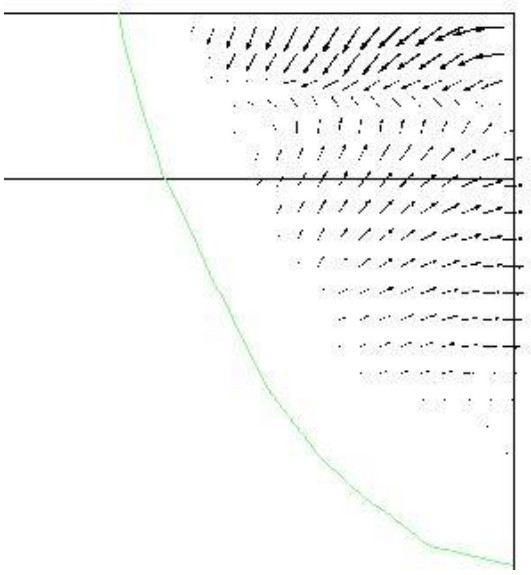

Fig. 13. Arrow Velocity Plot of Melt Pool Flow

The arrow velocity plot shows good agreement with the expected flow pattern of Marangoni flow, which should flow outwards towards the edge of the melt pool on the top surface where the flow begins to push downwards then loop back around along the melt pool boundary to the surface.

An advantage of this model compared to other models in the literature is that it gives a predictive cross section of the final bead. Figure 14 shows the model output next to an experimental cross section.

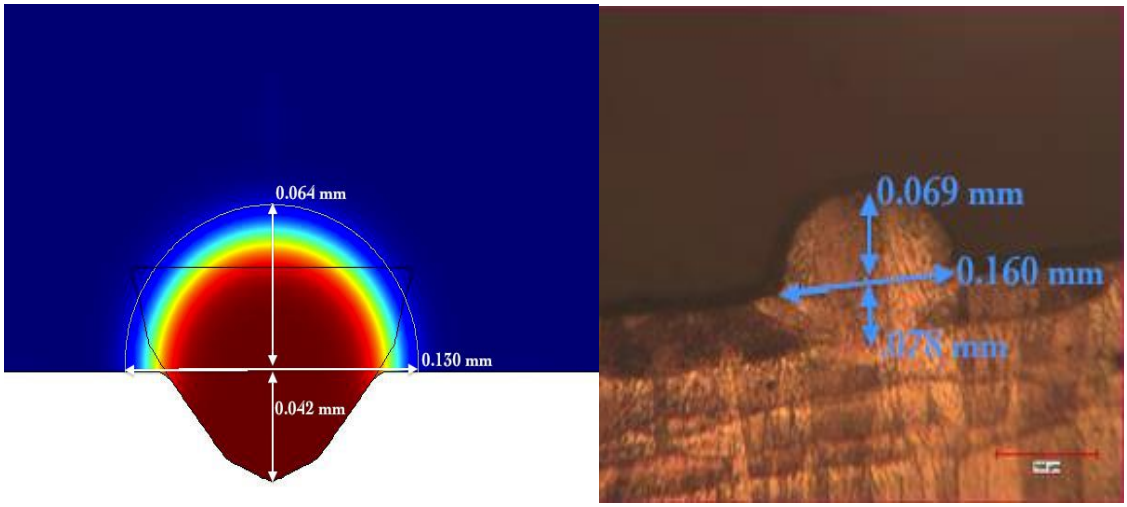

Fig. 14. Simulation and Experimental Cross Sections for 150W 700 mm/s

This type of complete bead geometry prediction is an upgrade from typical models which only consider thermal transport in a static block, and cannot predict geometry after the bead has fully formed. The black outline in the first picture of Figure 14 is the cross section that gets imported in from the three dimensional model. Before the bead solidifies it wets to the substrate and becomes dome shaped due to surface tension and gravity forces.

Chapter 5. Conclusion

A sophisticated and first of its kind FE model of the powder bed laser melting process has been developed. Unlike previous works this model directly simulates the Marangoni flow in the melt pool which negates the need for effective thermal conductivities and related assumptions. This simulation is made possible by an innovative technique deemed the forced rigidity method which involves modeling the entire block as a fluid and utilizing a temperature dependent dynamic viscosity. The temperature dependent dynamic viscosity allows elements below the melting

temperature of the modeled material to behave as a solid, while elements above the melting temperature are allowed to flow freely.

Furthermore this work offers a method to predict complete bead geometry after it has formed under surface tension and gravity forces. This method involves importing a 2 dimensional cross section of the melt pool from more common 3 dimensional models, then utilizes the level set method to track the interface between the molten bead and surrounding atmosphere.

This work used thermal conductivity values that were measured in lab using a TPS 2200 scientific instrument to ensure accuracy. Further work on this project should focus on the inclusion of a mass source into the model to simulate the powder that gets sucked into the melt pool due to Marangoni flow. There is also research to be done on how the particle size distribution of a given powder effects its thermal properties, and ultimately the final geometry of the melt pool.

References

[1] D. L. D. Bourell, J. J. Beaman, M. C. Leu, and D. W. Rosen, "A brief history of additive manufacturing and the 2009 roadmap for additive manufacturing: looking back and looking ahead," *US-Turkey Work. ...*, no. 2, pp. 2005–2005, 2009.

[2] J.-P. Kruth, M. C. Leu, and T. Nakagawa, "Progress in Additive Manufacturing and Rapid Prototyping," *CIRP Ann. - Manuf. Technol.*, vol. 47, no. 2, pp. 525–540, 1998.

[3] F. P. W. Melchels, J. Feijen, and D. W. Grijpma, "A review on stereolithography and its applications in biomedical engineering," *Biomaterials*, vol. 31, no. 24, pp. 6121–6130, 2010.

[4] B. Vayre, F. Vignat, and F. Villeneuve, "Metallic additive manufacturing: state-of-the-art review and prospects," *Mech. Ind.*, vol. 13, no. 2, pp. 89–96, 2012.

[5] B. Mueller and D. Kochan, "Laminated object manufacturing for rapid tooling and patternmaking in foundry industry," *Comput. Ind.*, vol. 39, no. 1, pp. 47–53, 1999.

[6] H. H. Zhu, L. Lu, and J. Y. H. Fuh, "Study on Shrinkage Behaviour of Direct Laser Sintering Metallic Powder," *Proc. Inst. Mech. Eng. Part B J. Eng. Manuf.*, vol. 220, no. 2, pp. 183–190, 2006.

[7] D. D. Gu, W. Meiners, K. Wissenbach, and R. Poprawe, "Laser additive manufacturing of metallic components: materials, processes and mechanisms," *Int. Mater. Rev.*, vol. 57, no. 3, pp. 133–164, 2012.

[8] F. Verhaeghe, T. Craeghs, J. Heulens, and L. Pandelaers, "A pragmatic model for selective laser melting with evaporation," *Acta Mater.*, vol. 57, no. 20, pp. 6006–6012, 2009.

[9] J. P. Kruth, G. Levy, F. Klocke, and T. H. C. Childs, "Consolidation phenomena in laser

and powder-bed based layered manufacturing," *CIRP Ann. - Manuf. Technol.*, vol. 56, no. 2, pp. 730–759, 2007.

[10] D. Gu and Y. Shen, "Balling phenomena in direct laser sintering of stainless steel powder: Metallurgical mechanisms and control methods," *Mater. Des.*, vol. 30, no. 8, pp. 2903–2910, 2009.

[11] J. Kruth, P. Mercelis, J. Van Vaerenbergh, and T. Craeghs, "Feedback control of Selective Laser Melting," *Proc. 3rd Int. Conf. Adv. Res. Virtual Rapid Prototyp.*, pp. 1–7, 2007.

[12] D. Gu, Y. C. Hagedorn, W. Meiners, G. Meng, R. J. S. Batista, K. Wissenbach, and R. Poprawe, "Densification behavior, microstructure evolution, and wear performance of selective laser melting processed commercially pure titanium," *Acta Mater.*, vol. 60, no. 9, pp. 3849–3860, 2012.

[13] B. J. Keene, "Review of data for the surface tension of pure metals," *Int. Mater. Rev.*, vol. 38, no. 4, pp. 157–192, 1993.

[14] C. L. Chan, J. Mazumder, and M. M. Chen, "Effect of surface tension gradient driven convection in a laser melt pool: Three-dimensional perturbation model," *J. Appl. Phys.*, vol. 64, no. 11, pp. 6166–6174, 1988.

[15] X. He, J. W. Elmer, and T. Debroy, "Heat transfer and fluid flow in additive manufacturing," *J. Laser Appl.*, vol. 25, no. 5, p. 052006, 2005.

[16] M. A. Larosa, A. L. Jardini, C. A. D. C. Zavaglia, P. Kharmandayan, D. R. Calderoni, and R. Maciel Filho, "Microstructural and mechanical characterization of a custom-built implant manufactured in titanium alloy by direct metal laser sintering," *Adv. Mech. Eng.*, vol. 2014, 2014.

[17] B. Cheng and K. Chou, "Melt Pool Geometry Simulations for Powder-Based Electron

Beam Additive Manufacturing," *Proc. Solid Free. Fabr. Symp.*, pp. 644–654, 2013.

[18] I. Yadroitsev, I. Yadroitsava, P. Bertrand, and I. Smurov, "Factor analysis of selective laser melting process parameters and geometrical characteristics of synthesized single tracks," *Rapid Prototyp. J.*, vol. 18, no. 3, pp. 201–208, 2012.

[19] D. Gu, "Laser additive manufacturing of high-performance materials," *Laser Addit. Manuf. High-Performance Mater.*, no. Lm, pp. 1–311, 2015.

[20] S. Mohanty and J. H. Hattel, "Numerical model based reliability estimation of selective laser melting process," *Phys. Procedia*, vol. 56, no. C, pp. 379–389, 2014.

[21] C. H. Fu and Y. B. Guo, "3-Dimensional Finite Element Modeling of Selective Laser Melting Ti-6Al-4V Alloy," *Solid Free. Fabr. Symp.*, pp. 1129–1144, 2014.

[22] C. D. Boley, S. A. Khairallah, and A. M. Rubenchik, "Calculation of laser absorption by metal powders in additive manufacturing.," *Appl. Opt.*, vol. 54, no. 9, pp. 2477–82, 2015.

[23] I. A. Roberts, C. J. Wang, R. Esterlein, M. Stanford, and D. J. Mynors, "A three-dimensional finite element analysis of the temperature field during laser melting of metal powders in additive layer manufacturing," *Int. J. Mach. Tools Manuf.*, vol. 49, no. 12–13, pp. 916–923, 2009.

[24] A. Foroozmehr, M. Badrossamay, E. Foroozmehr, and S. Golabi, "Finite element simulation of selective laser melting process considering optical penetration depth of laser in powder bed," *Mater. Des.*, vol. 89, pp. 255–263, 2015.

[25] M. Rahman, W. K. H. Seah, and T. T. Teo, "The machinability of inconel 718," *J. Mater. Process. Technol.*, vol. 63, no. 1–3, pp. 199–204, 1997.

[26] A. Thomas, M. El-Wahabi, J. M. Cabrera, and J. M. Prado, "High temperature deformation of Inconel 718," *J. Mater. Process. Technol.*, vol. 177, no. 1–3, pp. 469–472,

2006.

[27] T. Kitagawa, a Kubo, and K. Maekawa, “Temperature and wear of cutting tools in high-speed machining of Incone1718 and Ti-6A1-6V-2Sn,” *Wear*, vol. 202, no. 2, pp. 142–148, 1997.

[28] N. K. Tolochko, M. K. Arshinov, A. V. Gusarov, V. I. Titov, T. Laoui, and L. Froyen, “Mechanisms of selective laser sintering and heat transfer in Ti powder,” *Rapid Prototyp. J.*, vol. 9, no. 5, pp. 314–326, 2003.

[29] Comsol, “Comsol Multiphysics User’s Guid,” no. 4, p. 3, 2012.

[30] K. C. Mills, *Recommended Values of Thermophysical Properties for Selected Commercial Alloys*. Woodhead Publishing, 2002.

[31] R. F. Brooks, A. P. Day, R. J. L. Andon, L. A. Chapman, K. C. Mills, and P. N. Quested, “Measurement of viscosities of metals and alloys with an oscillating viscometer,” *High Temp. - High Press.*, vol. 33, no. 1, pp. 73–82, 2001.

[32] K. Shah, I. U. Haq, S. A. Shah, F. U. Khan, M. T. Khan, and S. Khan, “Experimental Study of Direct Laser Deposition of Ti-6Al-4V and Inconel 718 by Using Pulsed Parameters,” vol. 2014, 2014.

[33] S. Sumin Sih and J. W. Barlow, “The Prediction of the Emissivity and Thermal Conductivity of Powder Beds,” *Part. Sci. Technol.*, vol. 22, no. 3, pp. 291–304, 2004.

[34] G. A. Greene, C. C. Finfrock, and T. F. Irvine, “Total hemispherical emissivity of oxidized Inconel 718 in the temperature range 300-1000??C,” *Exp. Therm. Fluid Sci.*, vol. 22, no. 3–4, pp. 145–153, 2000.

Appendix A Chemical Composition of Inconel 718

Element	Composition, wt %
Nickel (plus Cobalt) (Ni, Co)	50.00 - 55.00
Chromium (Cr)	17.00 - 21.00
Iron (Fe)	Balance
Niobium (plus Tantalum) (Nb, Ta)	4.75 - 5.50
Molybdenum (Mo)	2.80 – 3.30
Titanium (Ti)	0.65 – 1.15
Aluminum (Al)	0.20 – 0.80
Cobalt (Co)	1.00 max
Carbon (C)	0.08 max
Manganese (Mn)	0.35 max
Silicon (Si)	0.35 max
Phosphorus (P)	0.015 max
Sulfur (S)	0.015 max
Boron (B)	0.006 max
Copper (Cu)	0.30 max

Appendix B Material Properties

Thermal Conductivity

	4.24 g/cm^3	4.49 g/cm3	5.46 g/cm3
373.55 K	0.262 W/mK	0.386 W/mK	0.425 W/mK
423.75 K	0.266 W/mK	0.344 W/mK	0.411 W/mK
472.75 K	0.272 W/mK	0.358 W/mK	0.417 W/mK
523.15 K	0.277 W/mK	0.341 W/mK	0.426 W/mK
572.95 K	0.281 W/mK	0.347 W/mK	0.421 W/mK
623.15 K	0.216 W/mK	0.238 W/mK	0.335 W/mK
672.95 K	0.139 W/mK	0.160 W/mK	0.228 W/mK
722.95 K	0.095 W/mK	0.120 W/mK	0.169 W/mK
773.15 K	0.265 W/mK	0.302 W/mK	0.471 W/mK
823.35 K		0.359 W/mK	0.732 W/mK
873.55 K		0.411 W/mK	0.989 W/mK
923.55 K		0.497 W/mK	
973.55 K		0.672 W/mK	
1023.75 K		0.819 W/mK	

Heat Capacity

Temperature (K)	Heat Capacity (J/K kg)	Apparent Heat Capacity (J/K kg)
298.00	435	435
373.00	455	455
473.00	479	479
573.00	497	497
673.00	515	515
773.00	427	427
873.00	558	558
973.00	568	568
1073.00	680	680
1173.00	640	640
1273.00	620	620
1373.00	640	640
1443.00	650	2101.807229
1460.00	720	2171.807229
1520.00	720	2171.807229
1580.00	720	2171.807229
1609.00	720	2171.807229
1673.00	720	720
1773.00	720	720
1873.00	720	720

Density

Temperature (K)	Density (kg/m3)
298	8190
373	8160
473	8118
573	8079
673	8040
773	8001
873	7962
973	7925
1073	7884
1173	7845
1273	7806
1373	7767
1443	7727
1609	7400
1673	7340
1773	7250
1873	7160

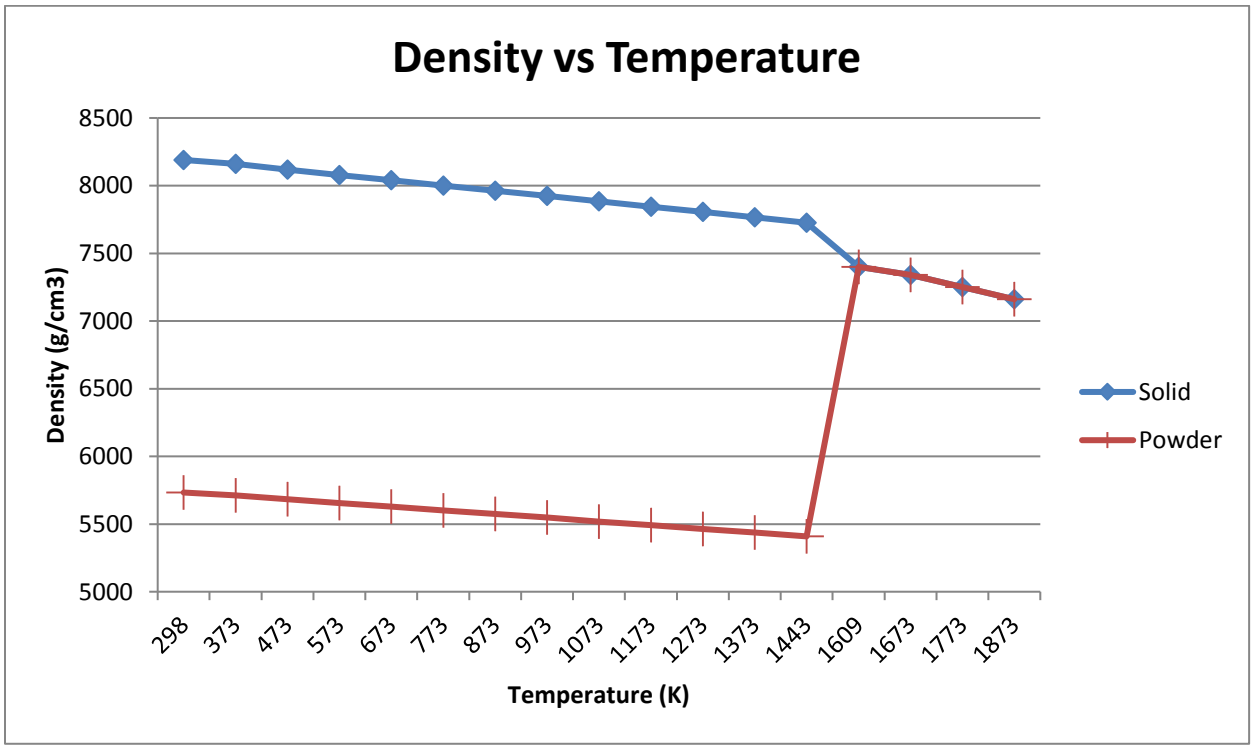

Dynamic Viscosity

Temperature (K)	Dynamic Viscosity (mPa*s)
1443	11.27995699
1473	10.38630767
1503	9.595020607
1533	8.891552916
1563	8.26377986
1593	7.701539713
1623	7.196273507
1653	6.740738055
1683	6.328776016
1713	5.955130601
1743	5.615295453
1773	5.305392385
1803	5.022071329
1833	4.762428058
1863	4.523936226
1893	4.304390986
1923	4.101862027
1953	3.914654283
1983	3.741274955
2013	3.580405712
2043	3.430879187
2073	3.291659025
2103	3.161822901